

CLOUD TRANSFORMERS

Kirill Mazur

Samsung AI Center Moscow

Skolkovo Institute of Science and Technology

Victor Lempitsky

ABSTRACT

We present a new versatile building block for deep point cloud processing architectures. This building block combines the ideas of self-attention layers from the transformer architecture with the efficiency of standard convolutional layers in two and three-dimensional dense grids. The new block operates via multiple parallel heads, whereas each head projects feature representations of individual points into a low-dimensional space, treats the first two or three dimensions as spatial coordinates and then uses dense convolution to propagate information across points. The results of the processing of individual heads are then combined together resulting in the update of point features. Using the new block, we build architectures for point cloud segmentation as well as for image-based point cloud reconstruction. We show that despite the dissimilarity between these tasks, the resulting architectures achieve state-of-the-art performance for both of them demonstrating the versatility of the new block.

1 INTRODUCTION

Convolutional neural networks (ConvNets) LeCun et al. (1989) and Transformers Vaswani et al. (2017) have emerged as the most successful data processing architectures across a variety of data domains. ConvNets are naturally suited for high-dimensional data that are sampled on low-dimensional grids and have spatial, temporal or spatial-temporal nature (e.g. images or sound). At the same time, Transformers scale less well to high-dimensional data but excel at handling less structured data such as phrases of a natural language.

In this work, we focus on *point clouds*, which are data of relatively high dimensionality but lacking the regularity of images. Despite the lack of the regularity and due to high dimensionality and spatial nature of point clouds, most state-of-the-art architectures for point cloud processing are derived from ConvNets. These ConvNet adaptations are based on direct rasterization of point clouds onto regular grids followed by convolutional pipelines Su et al. (2015b); Graham et al. (2018a), as well as on generalizations of the convolutional operators to irregularly sampled data Mao et al. (2019b); Wang et al. (2018) or non-rectangular grids Klokov & Lempitsky (2017); Jampani et al. (2016).

Here, we propose a new building block (a *cloud transform* block) for point cloud processing architectures that combines the ideas of ConvNets and Transformers (Figure 1). Similarly to the (self)-attention layers within transformers cloud transform blocks take unordered sets of vectors as an input, and process such input using multiple parallel *heads*. For an input set element, each head computes two- or three-dimensional *key* and a higher dimensional *value*, and then uses the computed keys to rasterize the respective values onto a regular grid. A two- or three-dimensional convolution is then used to propagate the information across elements. The results of parallel heads are then probed at key locations and are recombined together, producing an update to element features.

We show that multiple cloud transform blocks can be stacked sequentially and trained end-to-end, as long as special care is taken when implementing forward and backward pass through the rasterization operations. We then design *cloud transformer* architectures that concatenate multiple cloud transform blocks together with task-specific 3D convolutional layers. Specifically, we design a cloud transformer for semantic segmentation (which we evaluate on the S3DIS benchmark Armeni et al. (2016) and the ShapeNet-Part benchmark), and a cloud transformer for image-based geometric reconstruction (which we evaluate on a recently introduced ShapeNet based benchmark Tatarchenko* et al. (2019)). In the evaluation, the designed cloud transformers achieve state-of-the-art accuracy

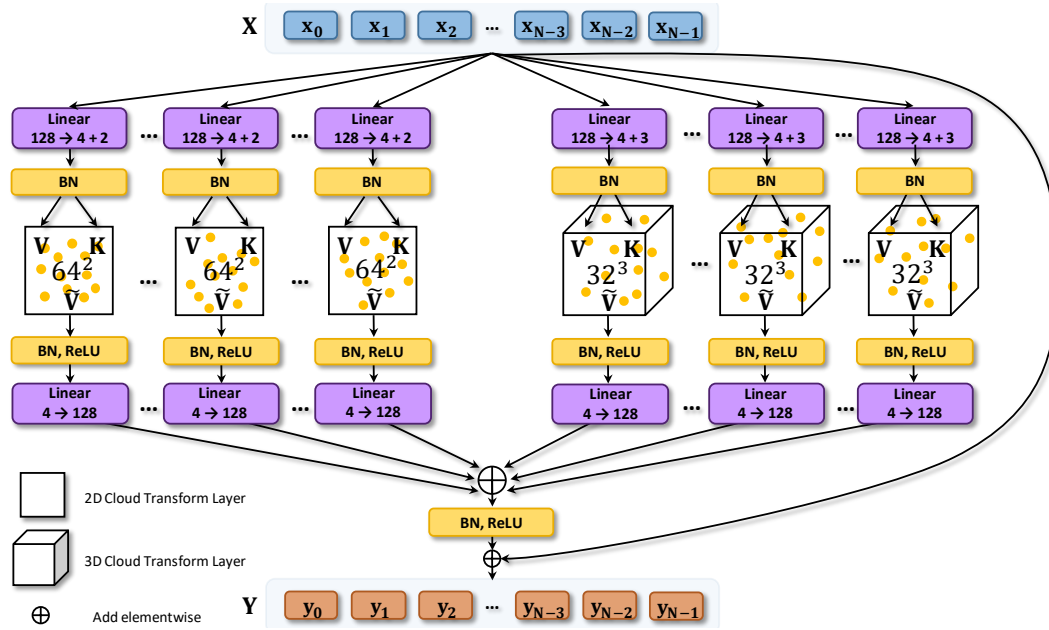


Figure 1: Our building block has several planar heads and several volumetric heads operating in parallel. Each head is a cloud transform, using a two-dimensional or a three-dimensional grid for rasterization, followed by convolutional operations, and de-rasterization (differentiable sampling).

for semantic segmentation task and considerably outperform state-of-the-art for image-based reconstruction. We note that such versatility is rare among previously introduced point cloud processing architectures, which can handle either recognition tasks (such as semantic segmentation) or generation tasks (such as image-based reconstruction) but usually not both.

2 RELATED WORK

Point cloud processing with deep architectures has grown to a large field of study. The ideas implemented within cloud transform blocks are closely related to a large body of prior works. Below, we review only the most related ones.

A number of work use rasterizations of the point cloud over regular 3D grids Maturana & Scherer (2015); Graham et al. (2018b); Moon et al. (2018); Mao et al. (2019a), where each point is rasterized at its original position within the point cloud. Multi-view ConvNets Su et al. (2015a) project point clouds to multiple predefined 2D views. The approaches that use splat convolutions on permutohedral grid convolutions Kiefel et al. (2015); Su et al. (2018) are perhaps most similar to ours (and have been an inspiration to us), as they also interleave rasterization (*splating*), (permutohedral) convolution, and probing (*slicing*). In contrast to all above-mentioned works, which use initial positions or data-independent projections of points for rasterizations, our architectures learn a variety of different and data-dependent projections (one projection per head in each block).

In Wang et al. (2019b), a dynamic graph ConvNet (DGCNN) architecture based on graph convolutions is presented. The graph is computed from spatial positions of the points that are modified in a data-dependent way within the architecture. In their case, the loss can not be backpropagated through the graph node position estimation since the spatial graph construction is non-differentiable. In contrast, our approach is based on regular grid convolutions and includes the backpropagation through position estimation (key computation). We also note that differentiable point cloud projection onto a 2D grid (from 3D space) has been used in Insafutdinov & Dosovitskiy (2018) though in a different way and for a different purpose than in our case.

Our approach is also strongly related to the seminal work on *spatial transformers* Jaderberg et al. (2015), which introduced blocks that warp signals on regular grids through data-dependent paramet-

ric warping and bilinear sampling. Our blocks also use bilinear sampling in the end of each head processing. Inspired by spatial transformers, Wang et al. (2019a) investigate how data-independent and data-dependent deformations of the original point clouds can be used to boost the performance of several recognition architectures including DGCNN Simonovsky & Komodakis (2017), SplatNet Su et al. (2018), and VoxelNet Zhou & Tuzel (2018). Similarly to Wang et al. (2019b) and unlike Jaderberg et al. (2015); Wang et al. (2019a) do not propagate the loss fully through deformation computation (in the case of data-dependent deformations). Compared to Wang et al. (2019a), our architectures employ regular 2D and 3D convolutions, can handle both recognition and generative tasks (the latter not considered in Wang et al. (2019a)), and are trained with gradient propagation through key position computation.

Transformer’s quadratic complexity have been recently addressed by sparse transformers Child et al. (2019) that alleviate the quadratic complexity of the original transformers in the set size, by restricting the interaction between elements in the set to predefined sparse subsets. Our mechanism based on rasterization and convolution can be seen as an alternative to sparse transformers that restricts interaction to elements that have been projected into adjacent grid cells.

3 METHOD

We proceed by first defining the key operation in our point processing pipeline that we call *cloud transform*. We then discuss how it can be embedded in a multi-head processing block. We finalize the section by discussing the architectures for point cloud segmentation and for image-based geometry reconstruction.

3.1 CLOUD TRANSFORM

The cloud transform takes as an input an unordered set (to which we further refer as point cloud) $X = \{\mathbf{x}_1, \dots, \mathbf{x}_N \mid \mathbf{x}_i \in \mathbb{R}^f\}$, whose elements are vectors $\mathbf{x}_i \in \mathbb{R}^f$ of a potentially high dimension f . The Cloud Transform $\mathcal{T}(X)$ maps such input into a new g -dimensional point cloud $Y \in \mathbb{R}^{N \times f}$ of the same size N . In other words, each point $\mathbf{x}_i \in X$ gets transformed into a new point $\mathbf{y}_i \in Y$. When designing such transform, one might want every point $\mathbf{y}_i \in Y$ to be dependent on the whole set X . Even though this property holds for the self-attention operation in Vaswani et al. (2017), this becomes problematic in the case of large set size because of quadratic complexity.

The cloud transform first applies a learnable projection \mathcal{P}_2 (further called *rasterization*), which generates a two-dimensional feature map with c channels, i.e. $\mathcal{P}_2: X \mapsto I \in \mathbb{R}^{w \times w \times c}$. Or, in a volumetric setting, the cloud transform starts with a learnable projection \mathcal{P}_3 , which generates a three-dimensional volumetric feature map, i.e. $\mathcal{P}_3: X \mapsto I \in \mathbb{R}^{w \times w \times w \times c}$. In both cases, w stands for the spatial resolution of the grid, while c stands for the number of channels.

Once an irregular point cloud X is projected onto a regular feature map, the cloud transform applies a single convolution or a more complex combination of convolutional operations. We denote the result of these convolutional layers as $\tilde{I} \in \mathbb{R}^{w \times w \times g}$ ($\tilde{I} \in \mathbb{R}^{w \times w \times w \times g}$ in the volumetric case). Note that we expect \tilde{I} to be of the same spatial size as I . However, the channel dimension of \tilde{I} might be changed from c to g .

The last step in our Cloud Transform operation is *de-rasterization* (also called *slicing*) $\tilde{\mathcal{P}}: \tilde{I} \rightarrow Y$ from the processed feature map \tilde{I} into a new *transformed* point cloud $Y \in \mathbb{R}^{N \times g}$. Note, that cloud transform passes information from \mathbf{x}_i to \mathbf{x}_j as long as these two points have been projected to sufficiently close positions. Thus, the cloud transform can be seen as a variant of self-attention layer with adaptive sparse attention mechanism. Below, for the sake of simplicity, we detail the steps of the cloud transform for a two-dimensional feature map case. The volumetric case is completely analogous.

Rasterization step. To rasterize each point \mathbf{x}_i , we predict the *value* $\mathbf{v}_i \in \mathbb{R}^c$ and the *key* $\mathbf{k}_i \in [0, 1]^2$. These two vectors stand for *what* to rasterize and *where* to rasterize respectively. In practice, this key-value prediction $\xi: \mathbf{x}_i \mapsto (\mathbf{v}_i, \mathbf{k}_i)$ can be implemented as a multi-layer perceptron (MLP) applied to the vector \mathbf{x}_i and producing a $(c+2)$ -dimensional vector. In our implementation, we use a single affine layer with the output dimension equal to six (i.e. $c=4$), followed by the

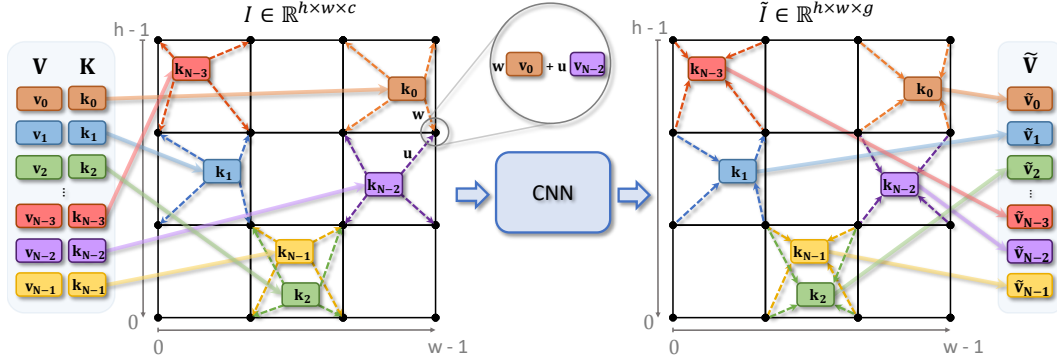


Figure 2: The cloud transform consists of rasterization (left) and de-rasterization(right) steps, with the convolutional part in between. It projects the high-dimensional point cloud onto low-dimensional (two-dimensional in this case) grid, applies convolutional processing, and lifts the result back to the high-dimensional space.

normalization layer. Depending on the architecture, the normalization layer can be batch normalization Ioffe & Szegedy (2015), instance normalization Ulyanov et al. (2017) or adaptive instance normalization Huang & Belongie (2017b). Finally, we apply clipping to the key values ensuring that all key values are between zero and one.

We then rasterize the value $v_i \in \mathbb{R}^c$ onto the grid $I = \mathbb{R}^{w \times w \times c}$ using the predicted key k_i as a position. Specifically, $k_i = (k_i^0, k_i^1) \in [0, 1]^2$ may be interpreted as a relative coordinate inside the spatial grid of I . Thus, the position defined by k_i falls into the enclosing integer cell $(h_0, w_0), (h_0, w_1), (h_1, w_0), (h_1, w_1)$, where $h_0 = \lfloor (w-1) \cdot k_i^0 \rfloor$, $h_1 = \lceil (w-1) \cdot k_i^0 \rceil$, $w_0 = \lfloor (w-1) \cdot k_i^1 \rfloor$, $w_1 = \lceil (w-1) \cdot k_i^1 \rceil$. The value v_i is then rasterized into four neighbouring feature map pixels $I[h_0, w_0], I[h_0, w_1], I[h_1, w_0], I[h_1, w_1] \in \mathbb{R}^c$ via bilinear assignment. In more detail, we compute bilinear weights $b_i = (b_i^{00}, b_i^{01}, b_i^{10}, b_i^{11})$ of the key k_i with respect to the cell it falls to:

$$\begin{aligned}
 b_i^{00} &= ((w-1) \cdot k_i^0 - h_1)((w-1) \cdot k_i^1 - w_1) \\
 b_i^{01} &= -((w-1) \cdot k_i^0 - h_1)((w-1) \cdot k_i^1 - w_0) \\
 b_i^{10} &= -((w-1) \cdot k_i^0 - h_0)((w-1) \cdot k_i^1 - w_1) \\
 b_i^{11} &= ((w-1) \cdot k_i^0 - h_0)((w-1) \cdot k_i^1 - w_0)
 \end{aligned} \tag{1}$$

The bilinear weights are then used to update the feature map I at corresponding locations:

$$\begin{aligned}
 I[h_0, w_0] &\leftarrow I[h_0, w_0] + b_i^{00} v_i \\
 I[h_0, w_1] &\leftarrow I[h_0, w_1] + b_i^{01} v_i \\
 I[h_1, w_1] &\leftarrow I[h_1, w_1] + b_i^{10} v_i \\
 I[h_1, w_0] &\leftarrow I[h_1, w_0] + b_i^{11} v_i
 \end{aligned} \tag{2}$$

The feature map I is initialized with zeros, and the rasterization is repeated for every $x_i \in X$, $i \in 1..N$ accumulating rasterized results at respective cells of the feature map I .

Convolution step. As discussed above, after rasterization, we transform the feature map I into \tilde{I} with any convolutional architecture that preserves the spatial resolution. Unless noted otherwise, we use a single convolutional layer that keeps the number of channels equal to four.

De-rasterization step. As the last step, we perform the *de-rasterization* transform $\tilde{\mathcal{P}}_2: \tilde{I} \rightarrow Y$ produces the transformed feature cloud Y using standard bilinear grid sampling operation. Thus, the transformed values $\tilde{I}[h_0, w_0], \tilde{I}[h_0, w_1], \tilde{I}[h_1, w_0], \tilde{I}[h_1, w_1] \in \mathbb{R}^g$ of the feature map are combined with bilinear weights $b_i = (b_i^{00}, b_i^{01}, b_i^{10}, b_i^{11})$ into the transformed value vector \tilde{v}_i . We apply the normalization layer, and the ReLU nonlinearity to the result of de-rasterization step, and further map each value from $c=4$ dimensions back to g dimensions ($g=128$ unless noted otherwise) using a learnable affine transform.

3.1.1 DENSITY NORMALIZATION

Surprisingly to us, Cloud Transform performs marginally better with no density normalization compared with its normalized counterpart. We find this particularly curious since this the converse holds for SPLATNet-like architectures.

Given spatial positions $P \in \mathbb{R}^{n \times 3}$, an auxiliary “density normalization“ term $\text{Conv}_g(\text{Splat}(P, 1))$ is introduced. This term consists of identity features 1, splatted (rasterized) at the positions P , which is $\text{Splat}(P, 1)$. It designed to approximate the uneven point cloud density. Finally, these densities are blurred with a Gaussian filter Conv_g . This step approximates a new density of the convolved features $\text{Conv}(\text{Splat}(P, F))$. The term is used prior to the slicing (de-rasterization) stage. We present a direct comparison with and without such normalization in our ablation studies section.

3.2 BACKPROPAGATION THROUGH CLOUD TRANSFORM

We have found that learning architectures with multiple sequentially-stacked Cloud Transform blocks via back-propagation Rumelhart et al. (1986) is highly unstable, as the gradients tend either to explode or vanish. The issue of exploding and vanishing gradients in deep neural networks has been thoroughly studied in Glorot & Bengio (2010); He et al. (2015). An ideal assumption on gradient variance during the back-propagation is to preserve its scale throughout the network.

In our case, the instability can be tracked to the gradient of the bilinear weights \mathbf{b} w.r.t. the key \mathbf{k} at the rasterization and de-rasterization steps. According to the chain rule, the gradients are multiplied by w during backpropagation through the keys.

Problem discussion Ultimately, the problem can be pinpointed to the fact that as the key \mathbf{k}_i moves from the top-left to the bottom-right of a certain grid cell thus traversing only $1/w$ -th of its variation range, the assignment weight of \mathbf{v}_i to the bottom-right corner changes from 0 to 1 (i.e traverses the full variation range). This means that gradients w.r.t. keys \mathbf{k}_i in our architecture will always be roughly w times stronger than w.r.t. values \mathbf{v}_i .

Gradient balancing trick Based on observation above, during back-propagation through keys, we simply divide the partial derivatives w.r.t. both coordinates of \mathbf{k}_i by w , i.e. we apply:

$$\frac{\partial \mathcal{L}}{\partial \mathbf{k}_i} \leftarrow \frac{1}{w} \frac{\partial \mathcal{L}}{\partial \mathbf{k}_i}. \quad (3)$$

We have found that this *gradient balancing* trick is sufficient to enable the learning of deep architectures containing multiple layers with cloud transforms.

Let us justify this trick by an exact derivation.

Lemma 1 Let $\mathbf{k} = (k_0, k_1) \in [0, 1]^2$ be a key, which is typically an output of the network’s key prediction branch in our Cloud Transform block. Let \mathbf{b} be a vector of bilinear weights of \mathbf{k} inside the enclosing cell, as in 3.1. The derivative of \mathbf{b} with the respect to \mathbf{k} is the following:

$$\frac{\partial \mathbf{b}}{\partial \mathbf{k}} = w \cdot \begin{pmatrix} (w \cdot k_1 - \lceil w \cdot k_1 \rceil) & (w \cdot k_0 - \lceil w \cdot k_0 \rceil) \\ -(w \cdot k_1 - \lfloor w \cdot k_1 \rfloor) & -(w \cdot k_0 - \lfloor w \cdot k_0 \rfloor) \\ -(w \cdot k_1 - \lceil w \cdot k_1 \rceil) & -(w \cdot k_0 - \lceil w \cdot k_0 \rceil) \\ (w \cdot k_1 - \lfloor w \cdot k_1 \rfloor) & (w \cdot k_0 - \lfloor w \cdot k_0 \rfloor) \end{pmatrix} \quad (4)$$

The derivation is straightforward, given the formula equation 1 for the bilinear weights. From the lemma above we see $\frac{\partial \mathbf{b}}{\partial \mathbf{k}} = w \cdot D$, where each element of the matrix D is bounded by 1 in absolute value. Thus, the back-propagation from bilinear weights \mathbf{b}_i to \mathbf{k}_i has a form:

$$\frac{\partial \text{Cost}}{\partial \mathbf{k}_i} = \left(\frac{\partial \mathbf{b}_i}{\partial \mathbf{k}_i} \right)^T \cdot \frac{\partial \text{Cost}}{\partial \mathbf{b}_i} = w \cdot D^T \cdot \frac{\partial \text{Cost}}{\partial \mathbf{b}_i} \quad (5)$$

Intuitively, the gradients are scaled up by w each layer during the fair back-propagation through the keys. Therefore, given a network with d cloud transform layers, the gradient norm would “explode”

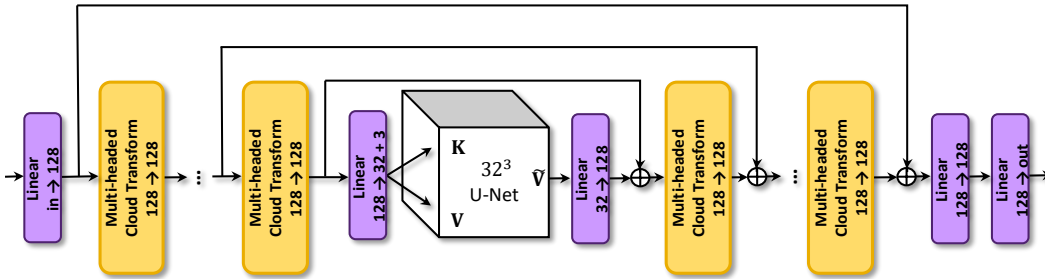


Figure 3: The architecture used for semantic segmentation is based on (1) ten standard multi-headed cloud transform blocks, followed by (2) a single-headed 3D cloud transform block with a deep Voxel-to-Voxel convolutional network, and (3) another sequence of ten standard multi-headed cloud transform blocks.

as w^d . We have observed such explosions experimentally. The balancing trick discussed above successfully fixes this problem.

3.3 MULTI-HEADED CLOUD TRANSFORM BLOCK

The rasterization and de-rasterization operation may lead to the information loss due to the limited number of nodes in two dimensional and three dimensional lattices (we use $w=64$ for two-dimensional grids and $w=32$ for three-dimensional grids). We therefore build our architectures from blocks that combine multiple cloud transforms operating in parallel. This is reminiscent of both the multiple self-attention head in the Transformer architecture Vaswani et al. (2017) and the multi-view convolutional networks Su et al. (2015a). Following Vaswani et al. (2017), we call each of the parallel cloud transform modules a *head* and thus consider a multi-head architecture. Each head predicts keys and values independently, and may use its own spatial resolution w . In fact, two-dimensional and three-dimensional heads can operate in parallel.

The results of the parallel heads for each point i are summed together, so that the resulting *multi-head cloud transform (MHCT) block* (Figure 1) still maps each input vector x_i to a g -dimensional vector y_i . We add another normalization layer and ReLU nonlinearity after the results of the heads are summed, and complete the block with the residual skip connection from the start to the end. He et al. (2015). We note that the multi-head cloud transform block also resembles the Inception block Szegedy et al. (2015), which uses heterogeneous parallel convolutions, as well as the blocks of the ResNeXt networks Xie et al. (2016), which use grouped convolutions with small number of channels in each group.

Unless noted otherwise, we use MHCT blocks with eight two-dimensional heads (with $w = 64$) and eight three-dimensional heads (with $w = 32$).

3.4 CLOUD TRANSFORMERS

We now discuss the architectures that can be constructed from MHCT blocks.

Semantic segmentation. The semantic segmentation cloud transformer (Figure 3) consists of an initial one-layer perceptron, which is applied to each point independently and transforms its 3D coordinates and 3D color features to an f -dimensional vector ($f=128$). Afterwards, we apply ten multi-headed cloud transform layers with default setting.

After the tenth MHCT layer, we insert a single cloud transform that enhances information propagation between distant points. This cloud transform uses volumetric grid with resolution $w=32$ and the feature dimensionality $c=32$. The convolutional part is a Voxel-to-Voxel Moon et al. (2018)-like with 4 downsampling and upsampling layers.

We then append ten more standard MHCT blocks. And then conclude the architecture with a two-layer shared perceptron that maps the features of each point to the logits of segmentation classes. Following the U-Net Ronneberger et al. (2015) idea, we add skip connections from the initial five

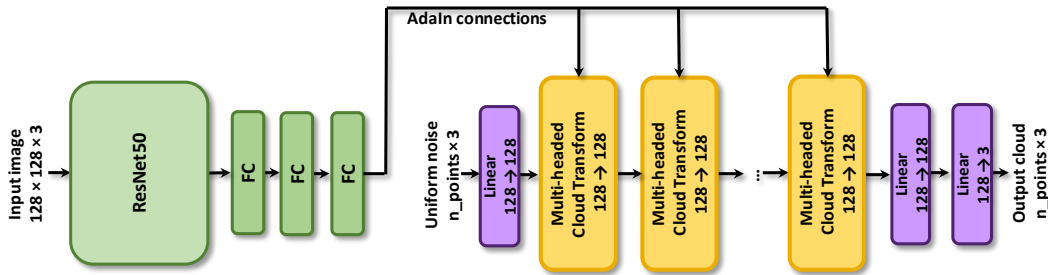


Figure 4: The architecture used for image-based reconstruction on fourteen standard multi-headed cloud transform blocks, conditioned via adaptive instance normalizations on the output of the convolutional encoder (green). The input to the first MHCT block is sampled from a uniform 3D distribution.

MHCT layers to the last five MHCT layers (the features passed through skip connections are merged through summation).

All normalization layers in the architectures are BatchNorm layers Ioffe & Szegedy (2015). The architecture has 7.2M parameters, of which 6.5M are in the central block. The architecture is trained with cross-entropy loss.

Point cloud generation. To create the architecture that generates point cloud, we stack 14 MHCT blocks sequentially, followed by a point-wise multi-layer perceptron that has two layers followed by *tanh* non-linearity that generates 3D points. The input point cloud is sampled from a uniform 3D distribution in the unit cube and then passed through point-wise linear layer, mapping each feature to $f=128$ dimensions.

To solve the image-based geometry reconstruction task (recovering point clouds from images), we use adaptive instance normalization (AdaIn) layers Huang & Belongie (2017a) in the MHCT blocks. We create image encoder with ResNet-50 architecture He et al. (2015) (pretrained on ILSVRC Rusakovsky et al. (2015)). The output of the encoder is a 512-dimensional vector, which is transformed into AdaIn coefficients via affine layer (Figure 4). The architecture is trained with earth mover distance (EMD) loss Liu et al. (2020).

4 EXPERIMENTS

Below, we report on the experiments with our architectures for the semantic segmentation and the image-based reconstruction tasks. We note that these tasks were chosen as arguably the most popular representatives of recognition and generation tasks respectively.

4.1 EXPERIMENTAL DETAILS.

We have observed that our model quality is sensitive to the first steps of optimizer, which is natural given the fact that our heads learn data projections into low-dimensional spaces.

We therefore used the RADAM optimizer Liu et al. (2019) with the learning rate 0.0001 for image-based reconstruction experiments and with the learning rate 0.001 for semantic segmentation experiments. We halve learning rate every 100k iterations for image-based reconstructions experiments and every 40k for semantic segmentation experiments. We observed similar performance with warmed-up ADAM optimizer Kingma & Ba (2015) (in which the learning rate is linearly increased from 0 to a target value typically within several thousands iterations), but in the end settled with RADAM in order to avoid setting of extra hyper-parameters. Our models were trained on four NVIDIA Tesla P40 GPU, with the batch size 16 per GPU.

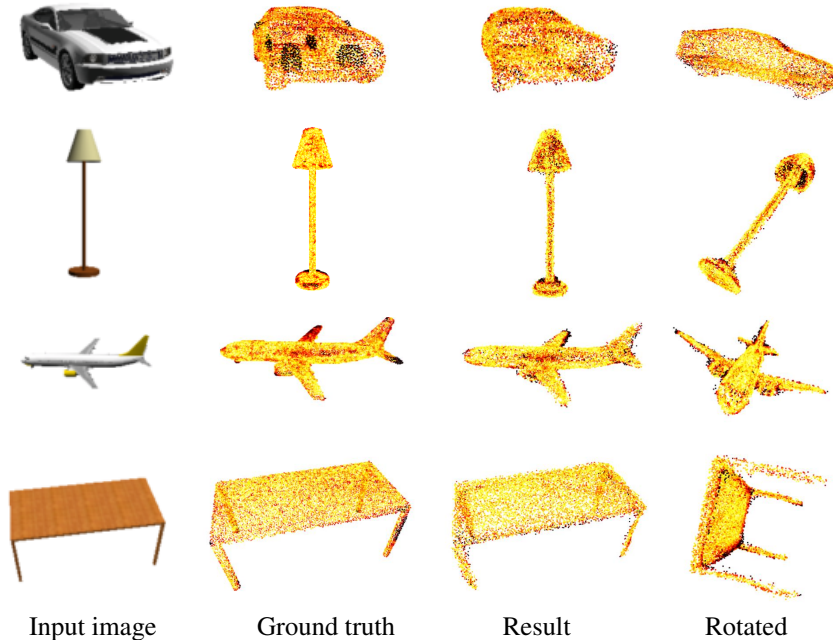


Figure 5: Sample image-based reconstruction obtained by our cloud transformer architecture. For each input, we show the ground truth, the result of the reconstruction (from the same viewpoint) and another view of the reconstruction. Note the ability of the cloud transformer to recover unseen parts despite being trained to reconstruct in the viewer-based coordinate frame, where reasoning about symmetries and object regularities is harder. Ground truth points are colored according to their distances to the reconstruction and *vice versa*.

4.2 SINGLE-VIEW OBJECT RECONSTRUCTION

In our generation experiments we follow the recently introduced benchmark Tatarchenko* et al. (2019) on 3D object reconstruction. The benchmark is based on ShapeNet Chang et al. (2015) renderings. Unlike previously ShapeNet-based benchmarks for image-based reconstruction that used *canonical coordinate frames* the new argues that the reconstruction should be evaluated in the *viewer-based coordinate frame*, where the task is more challenging and more realistic. The work Tatarchenko* et al. (2019) also provides evaluations of several recent methods on image-based reconstruction, as well as the retrieval-based oracle. The dataset consists of ShapeNet Chang et al. (2015) models, where each model belongs to one of 55 classes. Each object has been rendered with ShapeNet-Viewer from five random view points. We employ the same train/val/test split as Tatarchenko* et al. (2019).

In the benchmark, objects were rendered to 224×224 pixel images, which we resize to 128×128 pixels and then fed to our model. Our model outputs 8196 points to represent a reconstructed object in the viewer-aligned coordinate system. Since the protocol requires to predict exactly 10.000 points, we perform the reconstruction twice with different uniform noise and the same style vector z extracted by the encoder. This results in 16.392 points total from which we randomly select 10.000 points. We note that the ability to sample arbitrarily-large number of points is an attractive property of our architecture.

The main evaluation metric proposed in Tatarchenko* et al. (2019) is the F -score computed at a 1% volume distance threshold. The methods are compared with averaged per class F -score @1%, and by the number of classes, in which a method has the highest mean F -score @1%. Our quantitative results are summarized in Table 1. As can be seen, our method outperforms all methods evaluated in Tatarchenko* et al. (2019) *including* the retrieval-based oracle very significantly. We note that we have not performed extensive architecture search or hyperparameter tuning for this application, and it is very likely that another architecture based on our new block can achieve much better result.

Methods	avg. cl. F -score @1%	Top-1 cat.
AtlasNet	0.252	2
Matryoshka	0.217	3
OGN	0.264	2
Retrieval	0.236	0
Retrieval (<i>oracle</i>)	0.290	7
Cloud Transformer Cubic (ours)	0.367	47
Cloud Transformer Sphere (ours)	0.373	N\A

Table 1: F -score evaluation (@1%) of 3D shape reconstruction in the viewer-based coordinate frame. The cloud transformer outperforms other methods including the retrieval based oracle considerably. Only the cubic version is compared by the number of Top-1 categories for clarity, though the spherical version achieves similar performance.

We additionally observed an improvement in performance with a different type of noise feed to our model. Instead of a random point cloud sampled uniformly from a three-dimensional cube $[0, 1]^3$, the points are uniformly sampled from a unit sphere $S^2 \subset \mathbb{R}^3$. We speculate this is because most of the ShapeNet objects is two-dimensional manifolds in contrast with a three-dimensional filled cube.

In Figure 5, we provide several qualitative examples of input-output pairs, and note the ability of our method to recover fine details and to infer symmetries.

4.3 INDOOR SEMANTIC SEGMENTATION

The Stanford Indoor Dataset (S3DIS) Armeni et al. (2016) is a popular 3D point cloud segmentation benchmark that consists of large 3D point cloud scenes captured at three different buildings annotated with 13 semantic labels at the point level. The dataset comes with six splits.

For the sake of fair comparison, we evaluate on S3DIS using a conventional protocol, established by Qi et al. (2017a), which chunks rooms into $1m \times 1m$ blocks. Each block consists of 4096 points and each point is represented with its position xyz and its color, which results in a six-dimensional input vector. Following many previous works, we evaluate on ‘Area 5’ split and train on the remaining five splits, as Tchapmi et al. (2017b) advocate this fold as representative in measuring generalization ability due to Area 5 being shot in a separate building.

Since current state-of-the-art-method KPConv Thomas et al. (2019), uses a different protocol, we also evaluate our model using their protocol. In this setting we also train a higher-capacity Cloud Transformer with two subsequent Voxel-to-Voxel 3D heads in the middle (instead of the single head in the default architecture). In the KPConv protocol at each step an input point cloud is dynamically sampled from sphere of 2m radius. During evaluation the same data strategy is applied together with voting.

In both protocols spatial coordinates xyz are augmented with random rotation, anisotropic scale, jitter and shifts. Whereas for color augmentation we use chromatic autocontrast, jitter and translation (following Choy et al. (2019)).

The result of the comparison with state-of-the-art are given in Table 2. Our cloud transformers achieve state-of-the-art performance in both protocols.

We also visualize the operation of our default model in Figure 6. Here, we show the keys of the points of a sample S3DIS chunk near the beginning of the architecture, in the middle Voxel-to-Voxel layer, and near the end of the architecture. Ground truth labels are used for color coding. It can be seen that the model uses rather diverse transforms within parallel heads in both multi-head blocks. In the penultimate layer, several heads collapse the cloud to a small area/volume. Such head therefore performs global information propagation and is similar to the PointNet-like block Qi et al. (2017a). Interestingly, in the middle layer, the point cloud is transformed with relatively little deformation as compared to the input. This is not encoded into the architecture in any way and emerges naturally.

Method	mIoU	ceil.	floor	wall	beam	col.	wind.	door	chair	table	book.	sofa	board	clut.
Pointnet Qi et al. (2017a)	41.1	88.8	97.3	69.8	0.1	3.9	46.3	10.8	52.6	58.9	40.3	5.9	26.4	33.2
SegCloud* Tchapmi et al. (2017a)	48.9	90.1	96.1	69.9	0.0	18.4	38.4	23.1	75.9	70.4	58.4	40.9	13.0	41.6
Eff 3D Conv Zhang et al. (2018)	68.3	79.8	93.9	69.0	0.2	28.3	38.5	48.3	71.1	73.6	48.7	59.2	29.3	33.1
TangentConv Tatarchenko et al. (2018)	52.6	90.5	97.7	74.0	0.0	20.7	39.0	31.3	69.4	77.5	38.5	57.3	48.8	39.8
RNN Fusion Ye et al. (2018)	63.9	92.3	98.2	79.4	0.0	17.6	22.8	62.1	74.4	80.6	31.7	66.7	62.1	56.7
SPGraph* Landrieu & Simonovsky (2018)	58.0	89.4	96.9	78.1	0.0	42.8	48.9	61.6	84.7	75.4	69.8	52.6	2.1	52.2
ParamConv Wang et al. (2018)	58.3	92.3	96.2	75.9	0.3	6.0	69.5	63.5	66.9	65.6	47.3	68.9	59.1	46.2
PointCNN Li et al. (2018b)	57.2	92.3	98.2	79.4	0.0	17.6	22.7	62.1	74.4	80.6	31.7	66.7	62.1	56.7
CT (ours) std. prot.	61.0	93.4	97.8	81.1	0.0	14.4	38.7	74.1	86.0	78.2	60.9	43.8	69.1	55.9
Minkowski32* Choy et al. (2019)	65.3	91.7	98.7	86.1	0.0	34.0	48.9	62.4	89.8	81.5	74.8	47.2	74.4	58.5
KPConv* Thomas et al. (2019)	67.1	92.8	97.3	82.4	0.0	23.9	58.0	69.0	91.0	81.5	75.3	75.4	66.7	58.9
CT (ours)*	66.6	93.9	97.4	83.3	0.0	26.9	58.6	77.0	88.7	78.2	71.2	67.5	66.6	56.9
CT2 (ours)*	67.4	93.6	97.5	83.6	0.0	34.5	54.5	78.2	89.1	79.5	73.4	69.1	64.6	58.5

Table 2: Semantic segmentation intersection-over-union scores on S3DIS *Area-5* split. The models without * use the standard protocol with chunking of the scene into blocks, while the models with * employ different protocols. Our default cloud transformer model is denoted ‘CT’, while the model with extra capacity is denoted ‘CT2’. Cloud transformers match or outperform state-of-the-art in both protocols (standard and KPConv’s).

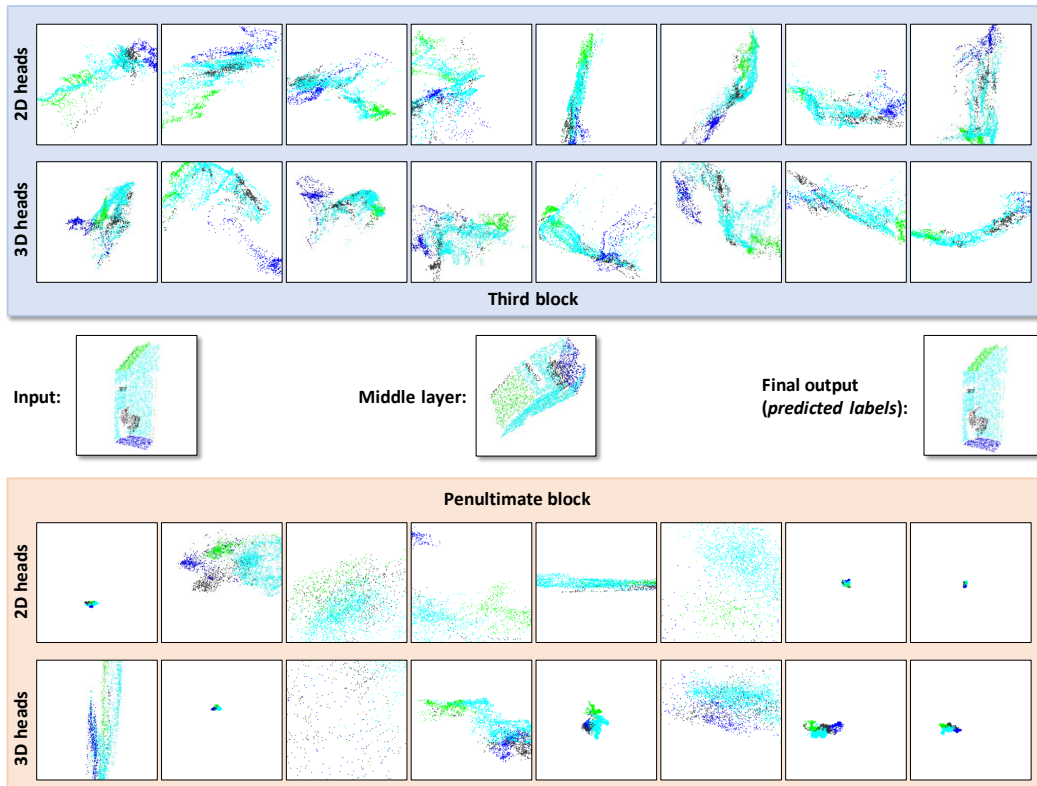


Figure 6: Information flow inside the segmentation architecture. Using the ground truth labels as color coding, we show the key locations inside the heads of the third block (top), the key locations inside the heads of the penultimate block (bottom), the key locations in the middle of the architecture (middle). The input example with ground truth labels is shown on the left, while the predicted labels are shown on the right (on top of the input point cloud). For 3D heads, we show projection of the keys on the XY coordinate plane. See text for discussion.

4.4 ABLATION STUDY

We also perform an ablation study to justify our architecture choices. We consider the following ablations:

- We add a **density normalization** term prior to the de-rasterization step, following the discussion in Section 3.1.1.
- We replace all learnable keys with different **non-learnable projections**. More precisely, in each head we apply a random affine transformation to the input point cloud, followed by the scaling with a logarithmically chosen scale. In case of the planar heads we also add a projection to the plane $z = 0$ before the scaling. This makes the method more similar to the SPLATNet architecture. It allows to verify our learnable key approach.
- In the **Coarser feature maps** experiment the spatial dimensions of feature maps are halved. Namely, volumetric heads of spatial sizes in MHCT are shrunked to 16^3 and planar heads to 32^2 .
- We also train an architecture **without planar heads** in order to see if using only volumetric heads might be sufficient.
- Furthermore, we consider a high-capacity variant with **no multihead** processing, where we use a single planar head with 32 channels (note that the capacity of each head is quadratic in the number of channels).
- Finally, we consider an architecture with **less layers**, replacing ten blocks in the beginning and ten blocks in the end of the architecture with six and six respectively.

As can be seen from Table 3, all ablated variants performed notably worse than the default architecture. These ablations also point out the possibility of improvement that can be easily achieved by e.g. increasing the number of MHCT blocks (at the cost of running on more parallel GPUs).

Methods	mIOU
Density norm.	55.1
Non-learnable proj.	55.9
Without planar heads	57.3
Coarser feature maps	58.5
No multihead	55.4
Less layers (6)	57.4
Cloud Transformer (full)	61.0

Table 3: Ablation study on Area 5 S3DIS conventional protocol. See text for discussion.

4.4.1 SHAPENETPART PART SEGMENTATION

We follow the protocol of SPH3D-GCN Lei et al. (2019) and train a separate network for each class. Our model architecture is the same as for the semantic segmentation, except for adding dropout regularization with rate 0.5 to the two last linear transformations in the network. Such regularization is needed due to a tiny train set size for some of the classes (e.g. rocket). The results are presented in Table 4. While in this benchmark our method does not exceed state-of-the-art, it performs essentially on par with it.

	instance mIoU	class mIoU	Air-plane	Bag	Cap	Car	Chair	Ear- phone	Guitar	Knife	Lamp	Laptop	Motor- bike	Mug	Pistol	Rocket	Skate- board	Table
# shapes			2690	76	55	898	3758	69	787	392	1547	451	202	184	283	66	152	5271
Kd-net Kulkov & Lempitsky (2017)	82.3	77.4	80.1	74.6	74.3	70.3	88.6	73.5	90.2	87.2	81.0	94.9	57.4	86.7	78.1	51.8	69.9	80.3
PointNet Qi et al. (2017a)	83.7	80.4	83.4	78.7	82.5	74.9	89.6	73.0	91.5	85.9	80.8	95.3	65.2	93.0	81.2	57.9	72.8	80.6
Spec-CNN Yi et al. (2016)	84.7	82.0	81.6	81.7	81.9	75.2	90.2	74.9	93.0	86.1	84.7	95.6	66.7	92.7	81.6	60.6	82.9	82.1
SPLATNet _{3D} Su et al. (2015a)	84.6	82.0	81.9	83.9	88.6	79.5	90.1	73.5	91.3	84.7	84.5	96.3	69.7	95.0	81.7	59.2	70.4	81.3
KCNet Shen et al. (2017)	84.7	82.2	82.8	81.5	86.4	77.6	90.3	76.8	91.0	87.2	84.5	95.5	69.2	94.4	81.6	60.1	75.2	81.3
SO-Net Li et al. (2018a)	84.9	81.0	82.8	77.8	88.0	77.3	90.6	73.5	90.7	83.9	82.8	94.8	69.1	94.2	80.9	53.1	72.9	83.0
PointNet++ Qi et al. (2017b)	85.1	81.9	82.4	79.0	87.7	77.3	90.8	71.8	91.0	85.9	83.7	95.3	71.6	94.1	81.3	58.7	76.4	82.6
SpiderCNN Xu et al. (2018)	85.3	81.7	83.5	81.0	87.2	77.5	90.7	76.8	91.1	87.3	83.3	95.8	70.2	93.5	82.7	59.7	75.8	82.8
SFCNN Rao et al. (2019)	85.4	82.7	83.0	83.4	87.0	80.2	90.1	75.9	91.1	86.2	84.2	96.7	69.5	94.8	82.5	59.9	75.1	82.9
PointCNN Li et al. (2018b)	86.1	84.6	84.1	86.5	86.0	80.8	90.6	79.7	92.3	88.4	85.3	96.1	77.2	95.3	84.2	64.2	80.0	82.3
Ψ -CNN Lei et al. (2019)	86.8	83.4	84.2	82.1	83.8	80.5	91.0	78.3	91.6	86.7	84.7	95.6	74.8	94.5	83.4	61.3	75.9	85.9
SPH3D-GCN Lei et al. (2019)	86.8	84.9	84.4	86.2	89.2	81.2	91.5	77.4	92.5	88.2	85.7	96.7	78.6	95.6	84.7	63.9	78.5	84.0
CT(ours)	86.1	84.8	84.3	88.3	88.0	81.7	90.6	79.9	91.3	88.8	84.6	96.2	78.5	95.7	83.8	62.1	79.8	83.8

Table 4: Part segmentation results on the ShapeNet Parts benchmark. Our results are very similar to the state-of-the-art.



Figure 7: Results of image-based reconstruction. Our network performs the reconstruction by sampling points from the unit cube and then “folding” this set into the answer. Here, we show the results, while coloring each point according to its initial position within the sphere (red, green, and blue values are used to color-code each coordinate).

5 CONCLUSION

We have presented a new block for neural architectures that process point clouds (and more generally vectorial sets). The new block has been encouraged by the success of Transformer architecture and its self-attention blocks, and harnesses the efficiency of 2D and 3D grid convolutions in modern parallel processors, GPUs in particular.

Based on the new block, we have presented architectures for point cloud semantic segmentation and single-image based geometry reconstruction that achieve state-of-the-art results. Additionally, we evaluated our model on a part segmentation dataset with a quality compatible with state-of-the-art. Between these three applications, it is perhaps the ability of our building block to perform well for generative tasks that is more interesting, and in the future we would like to investigate the performance of our approach for generation tasks. Our reconstruction architecture can be retargeted for other generation tasks easily by changing the encoder part.

REFERENCES

- Iro Armeni, Ozan Sener, Amir R. Zamir, Helen Jiang, Ioannis Brilakis, Martin Fischer, and Silvio Savarese. 3d semantic parsing of large-scale indoor spaces. In *Proc. CVPR*, 2016.
- Angel X. Chang, Thomas Funkhouser, Leonidas Guibas, Pat Hanrahan, Qixing Huang, Zimo Li, Silvio Savarese, Manolis Savva, Shuran Song, Hao Su, Jianxiong Xiao, Li Yi, and Fisher Yu. ShapeNet: An Information-Rich 3D Model Repository. Technical Report arXiv:1512.03012 [cs.GR], Stanford University — Princeton University — Toyota Technological Institute at Chicago, 2015.
- Rewon Child, Scott Gray, Alec Radford, and Ilya Sutskever. Generating long sequences with sparse transformers. *CoRR*, abs/1904.10509, 2019.
- Christopher Bongsoo Choy, JunYoung Gwak, and Silvio Savarese. 4d spatio-temporal convnets: Minkowski convolutional neural networks. *Proc. CVPR*, pp. 3070–3079, 2019.

- Xavier Glorot and Yoshua Bengio. Understanding the difficulty of training deep feedforward neural networks. In *AISTATS*, 2010.
- Benjamin Graham, Martin Engelcke, and Laurens van der Maaten. 3d semantic segmentation with submanifold sparse convolutional networks. In *Proc. CVPR*, 2018a.
- Benjamin Graham, Martin Engelcke, and Laurens van der Maaten. 3d semantic segmentation with submanifold sparse convolutional networks. *Proc. CVPR*, pp. 9224–9232, 2018b.
- Kaiming He, Xiangyu Zhang, Shaoqing Ren, and Jian Sun. Delving deep into rectifiers: Surpassing human-level performance on imagenet classification. *Proc. ICCV*, pp. 1026–1034, 2015.
- Xun Huang and Serge J. Belongie. Arbitrary style transfer in real-time with adaptive instance normalization. *Proc. ICCV*, pp. 1510–1519, 2017a.
- Xun Huang and Serge J. Belongie. Arbitrary style transfer in real-time with adaptive instance normalization. *Proc. ICCV*, pp. 1510–1519, 2017b.
- Eldar Insafutdinov and Alexey Dosovitskiy. Unsupervised learning of shape and pose with differentiable point clouds. In *Proc. NeurIPS*, pp. 2802–2812. 2018.
- Sergey Ioffe and Christian Szegedy. Batch normalization: Accelerating deep network training by reducing internal covariate shift. In *Proc. ICML*, volume 37, pp. 448–456, 2015.
- Max Jaderberg, Karen Simonyan, Andrew Zisserman, and koray kavukcuoglu. Spatial transformer networks. In *Proc. NIPS*, pp. 2017–2025. 2015.
- Varun Jampani, Martin Kiefel, and Peter V. Gehler. Learning sparse high dimensional filters: Image filtering, dense crfs and bilateral neural networks. In *Proc. CVPR*, June 2016.
- Martin Kiefel, Varun Jampani, and Peter V. Gehler. Permutohedral lattice cnns. In *ICLR Workshop Track*, May 2015. URL <http://arxiv.org/abs/1412.6618>.
- Diederick P Kingma and Jimmy Ba. Adam: A method for stochastic optimization. In *International Conference on Learning Representations (ICLR)*, 2015.
- Roman Klokov and Victor S. Lempitsky. Escape from cells: Deep kd-networks for the recognition of 3d point cloud models. *Proc. ICCV*, pp. 863–872, 2017.
- Loïc Landrieu and Martin Simonovsky. Large-scale point cloud semantic segmentation with super-point graphs. *Proc. CVPR*, pp. 4558–4567, 2018.
- Y. LeCun, B. Boser, J. S. Denker, D. Henderson, R. E. Howard, W. Hubbard, and L. D. Jackel. Backpropagation applied to handwritten zip code recognition. *Neural Comput.*, 1(4):541–551, December 1989. ISSN 0899-7667.
- Huan Lei, Naveed Akhtar, and Ajmal Mian. Octree guided cnn with spherical kernels for 3d point clouds. *IEEE Conference on Computer Vision and Pattern Recognition*, 2019.
- Jiabin Li, Ben M. Chen, and Gim Hee Lee. So-net: Self-organizing network for point cloud analysis. *2018 IEEE/CVF Conference on Computer Vision and Pattern Recognition*, pp. 9397–9406, 2018a.
- Yangyan Li, Rui Bu, Mingchao Sun, Wei Wu, Xinhan Di, and Baoquan Chen. Pointcnn: Convolution on x-transformed points. In S. Bengio, H. Wallach, H. Larochelle, K. Grauman, N. Cesa-Bianchi, and R. Garnett (eds.), *Proc. NeurIPS*, pp. 820–830. 2018b.
- Liyuan Liu, Haoming Jiang, Pengcheng He, Weizhu Chen, Xiaodong Liu, Jianfeng Gao, and Jiawei Han. On the variance of the adaptive learning rate and beyond. *ArXiv*, abs/1908.03265, 2019.
- Minghua Liu, Lu Sheng, Shilin Yang, Jing Shao, and Shi-Min Hu. Morphing and sampling network for dense point cloud completion. In *AAAI*, 2020.
- Jiageng Mao, Xiaogang Wang, and Hongsheng Li. Interpolated convolutional networks for 3d point cloud understanding. In *Proc. ICCV*, October 2019a.

- Jiageng Mao, Xiaogang Wang, and Hongsheng Li. Interpolated convolutional networks for 3d point cloud understanding. *Proc. ICCV*, pp. 1578–1587, 2019b.
- Daniel Maturana and Sebastian A. Scherer. Voxnet: A 3d convolutional neural network for real-time object recognition. In *Proc. IROS*, pp. 922–928. IEEE, 2015.
- Gyeongsik Moon, Ju Yong Chang, and Kyoung Mu Lee. V2v-posenet: Voxel-to-voxel prediction network for accurate 3d hand and human pose estimation from a single depth map. *Proc. CVPR*, pp. 5079–5088, 2018.
- Charles Ruizhongtai Qi, Hao Su, Kaichun Mo, and Leonidas J. Guibas. Pointnet: Deep learning on point sets for 3d classification and segmentation. *Proc. CVPR*, pp. 77–85, 2017a.
- Charles Ruizhongtai Qi, Li Yi, Hao Su, and Leonidas J. Guibas. Pointnet++: Deep hierarchical feature learning on point sets in a metric space. In *NIPS*, 2017b.
- Yongming Rao, Jiwen Lu, and Jie Zhou. Spherical fractal convolutional neural networks for point cloud recognition. *2019 IEEE/CVF Conference on Computer Vision and Pattern Recognition (CVPR)*, pp. 452–460, 2019.
- O. Ronneberger, P.Fischer, and T. Brox. U-net: Convolutional networks for biomedical image segmentation. In *Proc. MICCAI*, volume 9351 of *LNC3*, pp. 234–241, 2015.
- David E. Rumelhart, Geoffrey E. Hinton, and Ronald J. Williams. Learning representations by back-propagating errors. *Nature*, 323:533–536, 1986.
- Olga Russakovsky, Jia Deng, Hao Su, Jonathan Krause, Sanjeev Satheesh, Sean Ma, Zhiheng Huang, Andrej Karpathy, Aditya Khosla, Michael Bernstein, Alexander C. Berg, and Li Fei-Fei. ImageNet Large Scale Visual Recognition Challenge. *International Journal of Computer Vision (IJCV)*, 115(3):211–252, 2015. doi: 10.1007/s11263-015-0816-y.
- Yiru Shen, Chen Feng, Yaoqing Yang, and Dong Tian. Mining point cloud local structures by kernel correlation and graph pooling. *2018 IEEE/CVF Conference on Computer Vision and Pattern Recognition*, pp. 4548–4557, 2017.
- Martin Simonovsky and Nikos Komodakis. Dynamic edge-conditioned filters in convolutional neural networks on graphs. *Proc. CVPR*, pp. 29–38, 2017.
- Hang Su, Subhransu Maji, Evangelos Kalogerakis, and Erik G. Learned-Miller. Multi-view convolutional neural networks for 3d shape recognition. *Proc. ICCV*, pp. 945–953, 2015a.
- Hang Su, Subhransu Maji, Evangelos Kalogerakis, and Erik G. Learned-Miller. Multi-view convolutional neural networks for 3d shape recognition. In *Proc. ICCV*, 2015b.
- Hang Su, Varun Jampani, Deqing Sun, Subhransu Maji, Evangelos Kalogerakis, Ming-Hsuan Yang, and Jan Kautz. Splatnet: Sparse lattice networks for point cloud processing. *Proc. CVPR*, pp. 2530–2539, 2018.
- Christian Szegedy, Wei Liu, Yangqing Jia, Pierre Sermanet, Scott Reed, Dragomir Anguelov, Dumitru Erhan, Vincent Vanhoucke, and Andrew Rabinovich. Going deeper with convolutions. *Proc. CVPR*, pp. 1–9, 2015.
- Maxim Tatarchenko, Jaesik Park, Vladlen Koltun, and Qian-Yi Zhou. Tangent convolutions for dense prediction in 3d. In *Proc. CVPR*, pp. 3887–3896, 2018.
- Maxim Tatarchenko*, Stephan R. Richter*, René Ranftl, Zhuwen Li, Vladlen Koltun, and Thomas Brox. What do single-view 3d reconstruction networks learn? 2019.
- Lyne Tchammi, Christopher Choy, Iro Armeni, JunYoung Gwak, and Silvio Savarese. Segcloud: Semantic segmentation of 3d point clouds. In *International Conference on 3D Vision (3DV)*, pp. 537–547. IEEE, 2017a.
- Lyne P. Tchammi, Christopher Bongsoo Choy, Iro Armeni, JunYoung Gwak, and Silvio Savarese. Segcloud: Semantic segmentation of 3d point clouds. *International Conference on 3D Vision (3DV)*, pp. 537–547, 2017b.

- Hugues Thomas, Charles R. Qi, Jean-Emmanuel Deschaud, Beatriz Marcotegui, François Goulette, and Leonidas J. Guibas. Kpconv: Flexible and deformable convolution for point clouds. *Proc. ICCV*, pp. 6410–6419, 2019.
- Dmitry Ulyanov, Andrea Vedaldi, and Victor S. Lempitsky. Improved texture networks: Maximizing quality and diversity in feed-forward stylization and texture synthesis. *Proc. CVPR*, pp. 4105–4113, 2017.
- Ashish Vaswani, Noam Shazeer, Niki Parmar, Jakob Uszkoreit, Llion Jones, Aidan N. Gomez, Lukasz Kaiser, and Illia Polosukhin. Attention is all you need. In *Proc. NIPS*, 2017.
- Jiayun Wang, Rudrasis Chakraborty, and Stella X. Yu. Spatial transformer for 3d points. *ArXiv*, abs/1906.10887, 2019a.
- S. Wang, S. Suo, W. Ma, A. Pokrovsky, and R. Urtasun. Deep parametric continuous convolutional neural networks. In *Proc. CVPR*, pp. 2589–2597, 2018.
- Yue Wang, Yongbin Sun, Ziwei Liu, Sanjay E. Sarma, Michael M. Bronstein, and Justin M. Solomon. Dynamic graph cnn for learning on point clouds. *ACM Transactions on Graphics (TOG)*, 2019b.
- Saining Xie, Ross B. Girshick, Piotr Dollár, Zhuowen Tu, and Kaiming He. Aggregated residual transformations for deep neural networks. *Proc. CVPR*, pp. 5987–5995, 2016.
- Yifan Xu, Tianqi Fan, Mingye Xu, Long Zeng, and Yu Qiao. Spidercnn: Deep learning on point sets with parameterized convolutional filters. In *ECCV*, 2018.
- Xiaoqing Ye, Jiamao Li, Hexiao Huang, Liang Du, and Xiaolin Zhang. 3d recurrent neural networks with context fusion for point cloud semantic segmentation. In *Proc. ECCV*, pp. 415–430. Springer, 2018.
- Li Yi, Hao Su, Xingwen Guo, and Leonidas J. Guibas. Syncspecnn: Synchronized spectral cnn for 3d shape segmentation. *2017 IEEE Conference on Computer Vision and Pattern Recognition (CVPR)*, pp. 6584–6592, 2016.
- Chris Zhang, Wenjie Luo, and Raquel Urtasun. Efficient convolutions for real-time semantic segmentation of 3d point clouds. In *International Conference on 3D Vision (3DV)*, pp. 399–408. IEEE, 2018.
- Yin Zhou and Oncel Tuzel. Voxelnet: End-to-end learning for point cloud based 3d object detection. *Proc. CVPR*, pp. 4490–4499, 2018.

A APPENDIX

	AtlasNet	OGN	Matryoshka	Retrieval	Oracle NN	CT(ours)
airplane	0.39	0.26	0.33	0.37	0.45	0.49
ashcan	0.18	0.23	0.26	0.21	0.24	0.31
bag	0.16	0.14	0.18	0.13	0.15	0.21
basket	0.19	0.16	0.21	0.15	0.15	0.30
bath tub	0.25	0.13	0.26	0.22	0.26	0.30
bed	0.19	0.12	0.18	0.15	0.17	0.29
bench	0.34	0.09	0.32	0.3	0.34	0.49
birdhouse	0.17	0.13	0.18	0.15	0.15	0.55
bookshelf	0.24	0.18	0.25	0.2	0.2	0.34
bottle	0.34	0.54	0.45	0.46	0.55	0.61
bowl	0.22	0.18	0.24	0.2	0.25	0.31
bus	0.35	0.38	0.41	0.36	0.44	0.52
cabinet	0.25	0.29	0.33	0.23	0.27	0.42
camera	0.13	0.08	0.12	0.11	0.12	0.21
can	0.23	0.46	0.44	0.36	0.44	0.14
cap	0.18	0.02	0.15	0.19	0.25	0.12
car	0.3	0.37	0.38	0.33	0.39	0.44
cellular	0.34	0.45	0.47	0.41	0.5	0.56
chair	0.25	0.15	0.27	0.2	0.23	0.36
clock	0.24	0.21	0.25	0.22	0.27	0.40
dishwasher	0.2	0.29	0.31	0.22	0.26	0.22
display	0.22	0.15	0.23	0.19	0.24	0.41
earphone	0.14	0.07	0.11	0.11	0.13	0.35
faucet	0.19	0.06	0.13	0.14	0.2	0.31
file	0.22	0.33	0.36	0.24	0.25	0.40
guitar	0.45	0.35	0.36	0.41	0.58	0.60
helmet	0.1	0.06	0.09	0.08	0.12	0.1
jar	0.21	0.22	0.25	0.19	0.22	0.28
keyboard	0.36	0.25	0.37	0.35	0.49	0.38
knife	0.46	0.26	0.21	0.37	0.54	0.62
lamp	0.26	0.13	0.2	0.21	0.27	0.37
laptop	0.29	0.21	0.33	0.26	0.33	0.44
loudspeaker	0.2	0.26	0.27	0.19	0.23	0.33
mailbox	0.21	0.2	0.23	0.2	0.19	0.4
microphone	0.23	0.22	0.19	0.18	0.21	0.51
microwave	0.23	0.36	0.35	0.22	0.25	0.5
motorcycle	0.27	0.12	0.22	0.24	0.28	0.43
mug	0.13	0.11	0.15	0.11	0.17	0.20
piano	0.17	0.11	0.16	0.14	0.17	0.24
pillow	0.19	0.14	0.17	0.18	0.3	0.34
pistol	0.29	0.22	0.23	0.25	0.3	0.33
pot	0.19	0.15	0.19	0.14	0.16	0.26
printer	0.13	0.11	0.13	0.11	0.14	0.23
remote	0.3	0.33	0.31	0.31	0.37	0.45
rifle	0.43	0.28	0.3	0.36	0.48	0.48
rocket	0.34	0.2	0.23	0.26	0.32	0.2
skateboard	0.39	0.11	0.39	0.35	0.47	0.53
sofa	0.24	0.23	0.27	0.21	0.27	0.36
stove	0.2	0.19	0.24	0.18	0.19	0.33
table	0.31	0.24	0.34	0.26	0.34	0.43
telephone	0.33	0.42	0.45	0.4	0.5	0.46
tower	0.24	0.2	0.25	0.25	0.25	0.33
train	0.34	0.29	0.3	0.32	0.38	0.44
vessel	0.28	0.19	0.22	0.23	0.29	0.32
washer	0.2	0.31	0.31	0.21	0.25	0.23

Table 5: F-score evaluation (@1%) in the viewer-centered mode, per. class result for CT with the cubic noise.